Theses and Dissertations

2016

Physical Property Control In Core/Shell Inorganic Nanostructures For Fluorescence And Magnetic Targeting Applications

Stephen K. Roberts
University of South Carolina

PHYSICAL PROPERTY CONTROL IN CORE/SHELL INORGANIC
NANOSTRUCTURES FOR FLUORESCENCE AND MAGNETIC TARGETING
APPLICATIONS

by

Stephen K. Roberts

Bachelor of Science
Butler University, 2014

Submitted in Partial Fulfillment of the Requirements

For the Degree of Master of Science in

Chemistry

College of Arts and Sciences

University of South Carolina

2016

Accepted by:

Andrew B. Greytak, Director of Thesis

Richard D. Adams, Reader

Cheryl L. Addy, Vice Provost and Dean of the Graduate School

DEDICATION

This thesis is dedicated to:

My parents, Rick and Jeannie Roberts

and

My fiancée, Julia Gresik

ACKNOWLEDGEMENTS

ABSTRACT

Nanomaterials show immense promise for the future in numerous areas of application. Properties that are unique from the bulk material and are tunable allow for innovation in material design. This thesis will focus on controlling the physical properties of core/shell nanostructures to enhance the utility of the materials.

The first focus is on the impact of different solvent mixtures during the shell growth phase of SILAR based core/shell quantum dot synthesis is studied. Gaining insight into the mechanism for SILAR growth of core/shell nanoparticles allows improved synthetic yields and precursor binding, providing enhanced control to synthesis of core/shell nanoparticles. The second focus of this thesis is exploring the use of magnetic nanoparticles for magnetic drug targeting for to reduce the negative impact of cardiovascular conditions. Magnetic targeting for drug delivery enables increased local drug concentration, while minimizing non-specific interactions. In order to be effective for magnetic targeting, it must be shown that low magnetic strength is sufficient to capture flowing nanoparticles. By demonstrating the binding of a therapeutic agent to the surface at medicinal levels, the viability for use as a nanoparticle drug delivery system is improved.

TABLE OF CONTENTS

LIST OF FIGURES

ix

LIST OF ABBREVIATIONS

EED ....Excitation Energy Dependence

ML ....Monolayer

MMP ....Matrix Metalloproteinase

MRI ....Magnetic Resonance Imaging

NC .... Nanocrystal

PL .... Photoluminescence

PLE ....Photoluminescence Excitation

PLQY ....Photoluminescence Quantum Yield

PMAA .... poly(methacrylic acid)

QD ....Quantum Dot

QY ....Quantum Yield

SILAR .... Selective Ionic Layer Adsorption and Reaction

SPION ....Superparamagnetic Iron Oxide Nanoparticle

STEM .... Scanning Transmission Electron Microscopy

TCSPC .... Time-Correlated Single Photon Counting

CHAPTER 1

INTRODUCTION

1.1   Introduction to quantum dots

Quantum dots (QDs) are crystalline direct bandgap semiconductor nanoparticles, which are typically roughly spherical in shape and have a diameter on the order of 1-10 nm. The QDs can display properties that are unique from the bulk material, including quantum confinement in which the exciton Bohr radius is larger than all three crystal dimensions.[1] Quantum confinement of the excitons leads to desirable optical properties that can be tuned for utilization in lighting applications, photovoltaics, and bioimaging. Additionally, a higher bandgap semiconductor shell can be grown on the core, resulting in a core/shell heterostructure with increased isolation of the core and enhanced stability.

When semiconductors absorb light, an electron is excited from the valence band to the conduction band, creating a hole in the valence band. This electron-hole pair is known as an exciton. The relaxation of the electron will then result in either radiative or non-radiative recombination of the electron and hole. In radiative recombination, photons are emitted with energies near the bandgap (E_g) of the material. In contrast to bulk semiconductors, low dimensional materials, such as quantum dots, have discrete density of states and can thus be tuned by altering the size of the material. The size dependence of the bandgap absorption and emission makes these materials an attractive target for development in a number of industries including QD-based light emitting diodes[2,3] and fluorescent tags for biological imaging.[4,5]

1.1.1 Synthesis of quantum dots

In order to take advantage of the size dependent nature of the QDs, the synthesis method used must yield particles with a narrow size distribution and well-defined shape. The hot-injection method is the most widely used and consists of four stages.[6] The first involves mixing the two metal precursors at high temperature. The second stage occurs by quickly injecting chalcogenide precursors resulting in rapid nucleation. The third stage occurs when the nucleation rate has slowed and homogeneous growth of the QDs occurs. Finally, when the precursor concentration has decreased, small particles may dissolve and be redeposited on larger particles, which is known as Ostwald ripening. This results in an increased size distribution of particles. In order to prevent this process, the reaction should be quenched, either through lowering the temperature of the reaction or by introducing a protecting layer on the surface of the nanocrystals, prior to the ripening beginning.

As a result of an unpassivated surface and trap states, the quantum yield (QY) of core-only QDs is poor. Additionally, transference of an electron or a hole to a surface trap state is believed to be responsible for intermittency of photoluminescence, known as blinking, which poses a challenge to achieving reliable QYs.[7] Remediation of this issue can be achieved through the isotropic growth of shell material on the core,[8] effectively isolating the core from the surface trap states, reducing the wave function overlap with the surface, and decreasing the likelihood for surface trapping of the carriers.[9] Growth of thicker shells reduce Auger recombination rates, increasing multiexciton lifetimes and emissions, yielding a higher QY.[10,11] The lattice mismatch between the core and shell material must be minimized to prevent defect formation within the crystal structure,

2

which results in degraded performance. Graded alloy shells[12] and the use of materials with low lattice mismatch[13] have proven to be effective in minimizing defect density.

Two methods are commonly used for growth of a semiconductor material shell over a quantum dot core. The first method employs simultaneous addition of the precursors to form the shell. As the precursors used are highly reactive, this synthesis method exhibits limited control over the particle shape and a broad size distribution. The second method is selective ionic layer adsorption and reaction (SILAR). This method was first introduced by the Peng group[14] and has since been widely adopted. In contrast to simultaneous addition, SILAR introduces one precursor per half-cycle, allowing saturation of surface sites before the second precursor is introduced. The use of the SILAR technique benefits from greater control over shell thickness by selecting the number of addition cycles performed and decreased homogeneous nucleation events by eliminating precursor side reactions.[15]

1.2   Introduction to magnetic nanoparticle targeting

Magnetic nanoparticles exist in the size regime of less than 100 nanometers and have a high surface area to volume ratio.[16] In order to obtain desired physical and chemical properties in the particle, the core can be composed of numerous materials including gold, cobalt, iron oxide, or cadmium selenide. The tunability of the core material permits alteration and prioritization of properties, including size, shape, magnetic characteristics, biocompatibility, and solubility, to provides improved particles for various applications.[17] The applications that have been explored include magnetic

3

resonance imaging (MRI) contrast imaging,[18] magnetic hyperthermia,[19] magnetic drug delivery,[20–22] and data storage.[23]

While magnetic nanoparticles come in many combinations of materials, ferrimagnetic iron oxides, particularly magnetite (Fe_3O_4) and maghemite (γ-Fe_2O_3), are a popular core material for biomedical studies. One attractive property of iron oxide nanoparticles used for bioapplications is superparamagnetism, resulting in the particles often being referred to as superparamagnetic iron oxide nanoparticles (SPIONs). Superparamagnetism is typically exhibited in iron oxide particles smaller than 30 nm in diameter, allowing the magnetic moments to be flipped randomly by thermal energy, and resulting in paramagnetic nature only when a local magnetic field is applied to the nanoparticles.[16] This selective property leads a lower probability of aggregation of the nanoparticles in the bloodstream, as there is no remanent magnetism when a magnetic field is not actively being applied. As a softer magnetic material, iron oxide can also be magnetized or demagnetized with lower magnetic fields than what is required for harder magnetic materials. SPIONs possess a favorable toxicity profile, high magnetic susceptibility, and relatively high magnetic saturation, making them favorably suited for in vivo studies.[16]

1.2.1 Nanoparticle synthesis

The most widely used techniques for synthesis of magnetic nanoparticle include microemulsion, thermal decomposition, and coprecipitation techniques. Microemulsion syntheses can produce monodisperse particles, but typically have low yields, although new techniques have remedied this issue to a degree.[24] Many thermal decomposition

4

preparations are energy-intensive and require organic solvents, necessitating further processing to be made biocompatible.[25] Coprecipitation methods are typically performed in aqueous solution at room temperature, which results in increased size distribution and low crystallinity.[26] It is necessary for the synthesis to produce consistent nanoparticles, particularly with respect to SPIONs, as a wide distribution of particle size could lead to varied forms of magnetism amongst nanoparticles resulting in undesired magnetic characteristics. The most popular preparation method is a thermal technique developed by Hyeon et al. that is highly versatile and can form monodisperse nanocrystals in large quantities using inexpensive, non-toxic reactants.[27]

1.2.2 Nanoparticle surface

While the core material provides base functionality, coating the core with shell material, which can be performed in-situ or after synthesis, reduces aggregation of particles and can be used to enhance the functionality of the nanoparticles. Shell materials such as dextran, poly(ethylene glycol) (PEG), and silica are used to increase stability and introduce hydrophilicity to the particle, yielding increased solubility and enhanced biocompatibility.[28] Zwitterionic ligands bound to the core have also been shown to create suitably hydrophilic nanoparticles, while retaining the necessary magnetic properties. [29] The shell also plays an important role in biodistribution and how quickly the nanoparticles are cleared from the body. If the shell increases the hydrodynamic size of the nanoparticles above a threshold, the particles will be cleared more quickly through biological processes, reducing the availability of particles for the desired applications, and the magnetic properties of the cores could be diminished.[30]

5

Utilizing the characteristics from the core and shell, the nanoparticles can passively target an area for drug or MRI contrast agent delivery, employ ligands to attach to biological targets, or be used in magnetic targeting to concentrate the nanoparticles in a desired zone for drug release.[31,32] In order for nanoparticles that are injected into the blood stream to be effective for magnetic targeting, enough force must be exerted from a magnetic field gradient to overcome the effects of blood flow and pull the nanoparticles to the area of interest.[33] If the magnetic force is not sufficient to capture the SPIONs, they will continue in the bloodstream and be eliminated through non-specific pathways before they can accumulate at their targets.

1.3   Thesis overview

Chapter 2 is focused on understanding the effect of the solvent mixture on the growth of core/shell quantum dots using the SILAR technique. The inclusion of three different amines in the growth solvent is explored. The tertiary amine shows weaker association to the nanoparticle surface compared to the primary and secondary amines. Therefore, due to competition with precursors, use of tertiary amines during QD growth can increase the quality of the core/shell QDs.

The feasibility of iron oxide nanoparticles for use as a magnetically targeted drug delivery system is explored in Chapter 3. In vitro particle capture trials are performed via flow field fractionation on preliminary magnetic iron oxide nanoparticles to show the viability of capture by a readily-available magnet without the need for specialty high strength magnets. SiO_2 nanoparticles coated with poly(methacrylic acid) (PMAA) ligands are then used to explore the ability for a representative matrix metalloproteinase inhibitor

6

(MMPI) compound to be adsorbed to a functionalized nanoparticle surface. UV-Vis spectroscopy, in conjunction with centrifugation, is performed to determine the amount of drug binding occurring on the nanoparticle surface.

CHAPTER 2

REDUCING COMPETITION BY COORDINATING SOLVENT PROMOTES MORPHOLOGICAL CONTROL IN ALTERNATING LAYER GROWTH OF CDSE/CDS CORE/SHELL QUANTUM DOTS*

2.1 Introduction

The formation of core/shell structures in colloidal semiconductor nanocrystals is important in maintaining the spectroscopic properties of colloidal quantum dots (QDs) and defining new functions. When using selective ionic layer adsorption and reaction (SILAR)-based techniques, conversion of shell precursors to surface-adsorbed equivalents should be maximized for effective control of shell growth. Our group has previously demonstrated that the commonly used cadmium precursor Cd(oleate)$_2$ has low conversion yield when added in monolayer-equivalent quantities during the growth of CdSe/CdS core/shell QDs via the SILAR technique.[34] The growth solvent could potentially play an important role in governing precursor conversion.

Primary amines have been typically been used as the coordinating solvent for nanoparticle growth, with oleylamine commonly used for CdSe QDs growth by SILAR.[15,34] The role of the primary amine during growth has been well studied, yet contradictions have arisen between conclusions, as summarized by Garcia-Rodriguez et

---

* Tan, R.; Shen, Y.; Roberts, S. K.; Gee, M. Y.; Blom, D. A.; Greytak, A. B. *Chem. Mater.*, **2015**, 27 (21), 7468–7480. Reprinted here with permission of publisher.

8

www.manaraa.com

al.[35] Switching to secondary amines for CdS shell growth on CdSe cores has been reported to improve synthetic yield[36,37], while secondary and tertiary amines have shown improved size distribution during CdSe core growth.[38] One possible mechanism is that the reactivity of the Cd precursor was reduced due to the strong coordination of the primary amine. Liu's and Vela's groups have suggested[35,37] that primary amines such as oleylamine may stabilize $Cd(oleate)_2$ in solution through the formation of six-coordinate complexes. Solution-phase complexes could be sterically restricted in the case of secondary or tertiary amines.[37] However, it is also known that amines can improve the fluorescence quantum yield by coordination to the nanocrystal surface, and it is possible that such surface coordination is competing with precursor conversion.[39–41]

In this work, we grew CdSe/CdS core/shell quantum dots in solvent mixtures with three different representative amines -- primary, secondary, and tertiary -- via a SILAR technique. We selected oleylamine (OAM), dioctylamine (DOM), and trihexylamine (THM) for our studies. The three amines were chosen to (1) represent primary/secondary/tertiary amines, and (2) have similar molecular weight and molar volume, so that similar amine:QD ratios (∼50 000:1) could be achieved at similar QD concentrations. The course of the growth was monitored by UV−visible absorption and photoluminescence (PL) emission spectroscopy. Emission peaks at wavelengths shorter than the effective band gap ("blue peaks") appeared in the PL spectrum when QDs were grown in primary amine, suggesting nucleation of small CdS particles as a result of cross-reaction of the shell precursors as seen previously, and such nucleation was suppressed and no CdS particles were present in the QDs grown in tertiary amine. Time-correlated single photon counting (TCSPC) measurements indicated shorter average lifetimes and

9

increased rate dispersion in samples prepared with secondary and tertiary amines, when compared to oleylamine. This finding indicates a difference in interactions/passivation between the different amines and the QD surface. Scanning transmission electron microscopy (STEM) proved the yield of the shell was highest when using the tertiary amine (trihexylamine) as the growth solvent. We demonstrated that the interaction between the solvent molecules and the nanoparticle surface is an issue influencing shell growth by SILAR, because the shell precursor must compete with such interactions to saturate the surface prior to introduction of the complementary precursor for growth of the shell compound.

2.2   Shell growth as monitored by absorption and emission spectroscopy

During the course of the growth, aliquots with a consistent volume of 50 ± 5 μL were drawn and diluted in 2.0 ± 0.2 mL of hexane for monitoring by absorption and PL spectroscopy. This method resulted in diluted samples with <25% error in concentration. The nominal concentration of core/shell particles in each aliquot can be calculated on the basis of the quantity of cores introduced at the start of the reaction; the nominal concentration decreases over the course of shell growth due to the increase in total volume as shell precursor solutions are introduced. The band-edge absorbance peak of all aliquots remained less than 0.1 AU such that little fluorescence light is reabsorbed when the samples are excited. Absorption and PL spectra of core/shell particles grown in the three amines are shown in **Figure 2.1**. To facilitate comparison, the absorption and PL spectra of successive aliquots have been scaled to compensate for the difference in nominal concentration of core/shell particles. In particular, the absorbance and intensity

10

values plotted should be representative of the signals seen at the same QD concentration (0.42 μM), with a scaling error of less than 25%. In all three shell growth experiments, the absorption spectra indicate a red shift in the lowest-energy (1S) exciton resonance observed with increasing shell thickness, accompanied by an increase in the height of the scaled 1S absorbance. An increase in the 1S molar extinction coefficient with increasing size of CdSe QDs has been described and modeled by Jasieniak et al.[42] The trend for the same model applied to the evolution of the 1S absorbance in the CdSe/CdS core/shell particles is indicated by the black curves in **Figure 2.1A−C**, with 25% error indicated by dashed lines.

Figure 2.1D−F shows that in all three growths, the PL emission intensity of CdSe/CdS core/shell particles continuously increased with increasing CdS shell thickness. This is a result of an increasing quantum yield as well as an increasing excitation rate at the same concentration due to enhanced absorption at short wavelengths because of the CdS shell.

Despite superficially similar absorption spectra and band-edge PL spectra among the three samples, a close examination of the emission spectra reveals a PL peak appearing between 400 and 500 nm ("blue peak") that is present in the oleylamine case (**Figure 2.1D**), greatly diminished (∼50× less intense) with dioctylamine, and nearly absent with trihexylamine. The blue peaks are absent prior to introduction of shell precursors, are centered at wavelengths shorter than the emission of the CdSe cores used, and shift to longer wavelengths as additional shell precursors are introduced. These characteristics are all consistent with the appearance of a CdS nanoparticle side product. We have previously shown that nucleation of CdS nanoparticles can occur when growing

11

CdSe/CdS core/shell QDs via the SILAR technique under 1 ML equivalent dose per cycle.[34] The wavelengths of the blue peaks fall within the range of emissions for CdS nanoparticles with diameters of 3.5−4.5 nm.[43,44]
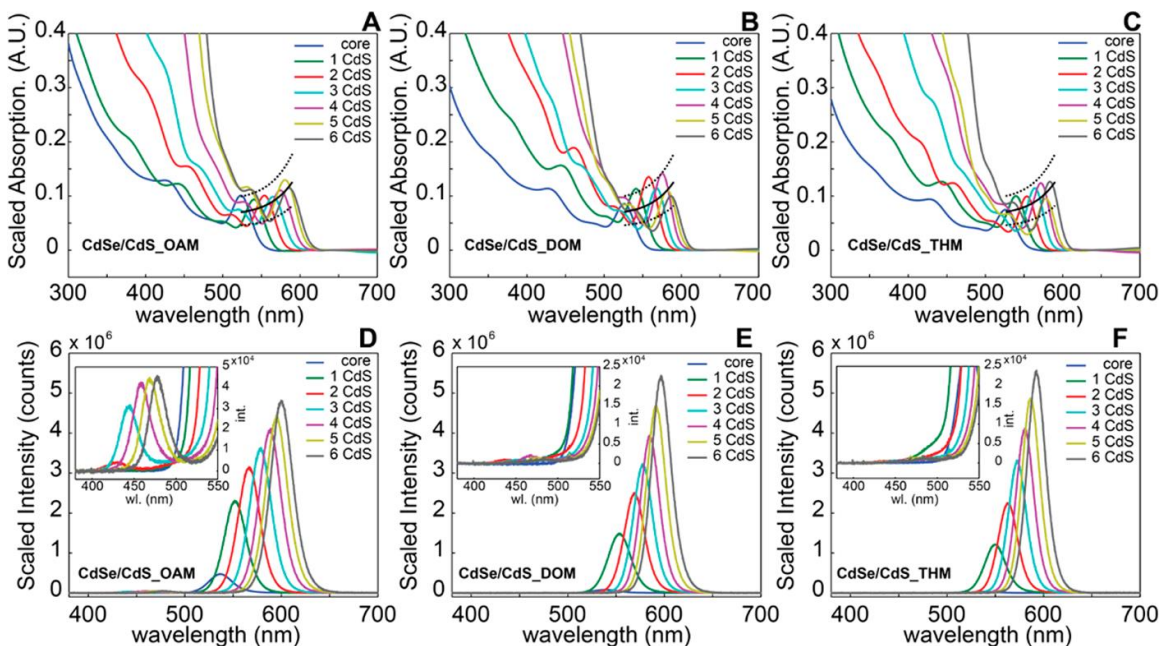

Figure 2.1 Scaled absorption and emission spectra over the course of CdSe/CdS core/shell QDs growth in three amines. (A,D) **CdSe/CdS_OAM** grown in oleylamine; (B,E) **CdSe/CdS_DOM** grown in dioctylamine; (C,F) **CdSe/CdS_THM** grown in trihexylamine. Absorptions and emissions are normalized to the concentration of QDs in each aliquot, so that all of the absorption and emission represent the absorption and intensity of the same amount of QDs; the dashed lines represent the upper and lower bands of 25% error for the QD concentration in each aliquot. The insets zoomed in the region of emission where "blue peaks" appeared for **CdSe/CdS_OAM** and **CdSe/CdS_DOM**, and no "blue peaks" in **CdSe/ CdS_THM**. Copyright 2015 American Chemical Society.

2.3   Characterization of the Presence/Absence of Nucleation by Photoluminescence Excitation Spectroscopy

We conducted photoluminescence excitation (PLE) scans on all three core/shell samples to characterize the contribution of CdS nanoparticle nucleation to the observed ensemble absorption spectra. The PLE spectrum measures the emission intensity as a function of excitation wavelength. For a QD in which all excitations are presumed to

rapidly thermalize to the band-edge exciton states, the PLE spectrum nominally contains the same information as the absorption spectrum. However, disconnected particles of the shell material as well as hot-carrier recombination processes will lead to a diminished PLE spectrum as compared to the absorption spectrum. Technically, the PLE signal should be compared to the number of photons absorbed by the sample at each wavelength, which is proportional to $1 - T$ where T is the optical transmittance.[45] The absorbance $A = -\log(T)$ is described accurately by $1 - T$ (within 10%) only when $A < 0.1$. To further minimize light attenuation considerations,[46] the samples were diluted by hexane so that in all cases the absorbance was <0.2 at wavelengths longer than 300 nm.[45]
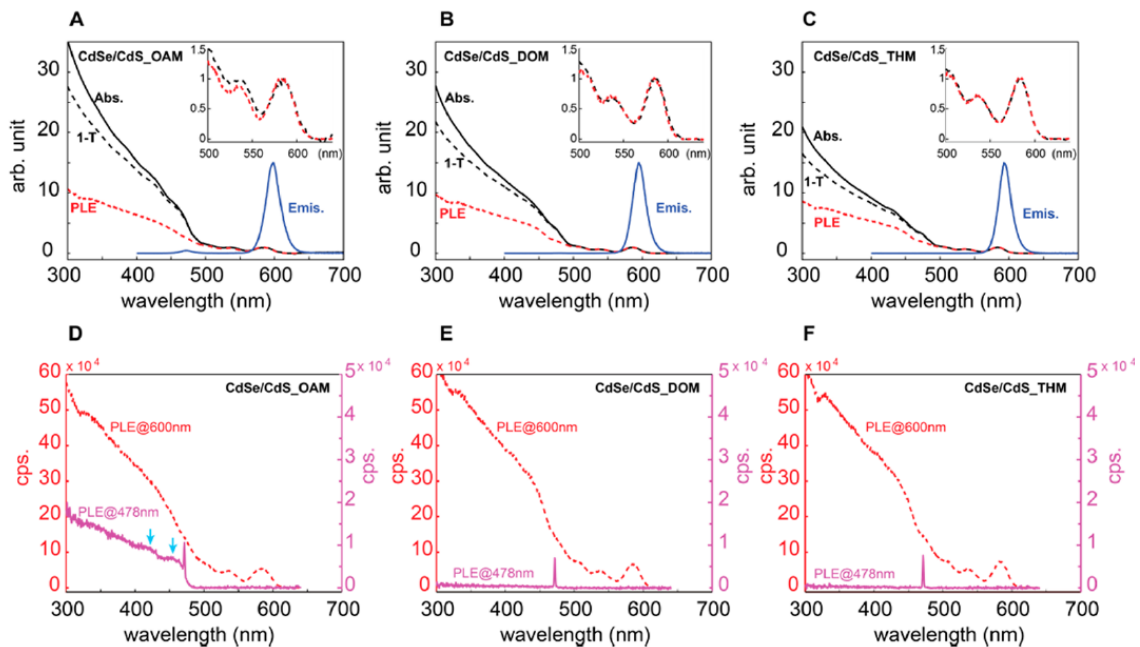
Figure 2.2 (A−C) Photoluminescence excitation (PLE) scans at emission maximum (@600 nm) for CdSe/CdS core/shell particles grown in three amines are shown as red dashed lines. PLE, absorption (black solid lines), and $1 - T$ (black dashed lines) are shown and normalized to the bandgap absorption peak for comparison. Normalized emissions are shown as a blue solid line. The insets show PLE and $1 - T$ at the bandgap. (D−F) Comparison of PLE scans at emission maximum (@600 nm, red dashed lines) and PLE scans at "blue peak" maximum (@478 nm, purple solid lines) for three core/shell particle samples. Copyright 2015 American Chemical Society.

13

In **Figure 2.2A−C**, the excitation wavelength was scanned from 300 to 640 nm, which covers the absorption range for typical CdS and CdSe nanoparticles, while the emission wavelength was set at the band-edge PL emission maximum (PLE@600 nm). At long wavelengths close to the band edge, the PLE line shape matches $1 - T$ closely as expected for the simple picture of a QD with energy-independent QY. Consequently, it is possible to scale the $1 - T$ and PLE signals such that they are superimposed in this region (**Figure 2.2A−C**, insets, with the lowest-energy exciton peak set at 1 on the vertical scale), so that differences at higher energies (shorter wavelengths) can be examined. For comparison, the raw absorbance signal A is plotted as well. At shorter wavelengths, the normalized $1 - T$ signal greatly exceeds the PLE trace in all samples, indicating a lower ensemble QY for excitation at high energies. Comparing the three samples, it is clear that in the low wavelength region (300−500 nm), the absorbance and $1 - T$ are the largest for CdSe/CdS_OAM, then CdSe/CdS_DOM, with CdSe/CdS_THM showing the lowest values, while PLEs@600 nm showed negligible differences. These results suggest that the additional absorbance seen in CdSe/CdS_OAM at shorter wavelengths does not contribute to band-edge emission. We propose that the additional absorbance in CdSe/CdS_OAM is contributed by the CdS nanoparticles that are responsible for blue emission peaks in the PL spectra. PLE scans with the emission wavelength set to 478 nm (PLE@478 nm, **Figure 2.2D,E**) showed a substantial signal from 300 to 480 nm for CdSe/CdS_OAM (**Figure 2.2D**) that was absent for CdSe/CdS_DOM and CdSe/CdS_THM. This signal displayed peaks (blue arrows in **Figure 2.2D**) resembling excitonic features of typical semiconductor nanoparticles as a result of quantum

confinement. The above observations are consistent with the optical properties expected for CdS nanoparticles.

Additional insight on the behavior of the samples under excitation at low wavelengths can be gained by subtracting the normalized PLE@600 nm spectrum from normalized $1 - T$. The difference represents photons being absorbed by the sample that do not lead to emission at 600 nm. The difference signals are overlaid in **Figure 2.3A** on a scale relative to the PLE signal at the lowest energy exciton that allows the values for the three samples to be directly compared. In all cases, a large difference signal grows in at wavelengths <500 nm. There are two possible contributions to the difference signals shown: first, inefficient relaxation of delocalized, higher-energy excited states to the band-edge exciton localized at the QD core; and second, photon absorption by detached CdS nanoparticles. The latter of these contributions should mimic the absorption spectrum of CdS QDs. **Figure 2.3B** shows that the profile of the $1 - T$ difference spectrum for CdSe/CdS_OAM differs from that of the other two. If the spectra are normalized at a wavelength near the onset of the excess $1 - T$ signal (**Figure 2.3C**), it is clear that the CdSe/CdS_OAM sample displays an additional contribution at shorter wavelengths with excitonic features that closely resemble what is expected for CdS QDs.[43,44] The remaining contribution that is common to all samples (although differing in amplitude) could be evidence of a rapid nonradiative trapping pathway for hot carriers. Providing excitation energy above the band gap results in a higher likelihood of accessing nonemissive trap states, resulting in a reduced quantum yield. Excitation energy dependence (EED) in CdSe and core/shell QDs has been observed previously.[47–49] Precautions should be taken to avoid the effects of EED when examining QDs in future

studies. Additional understanding of EED could provide insight into improved methodology.
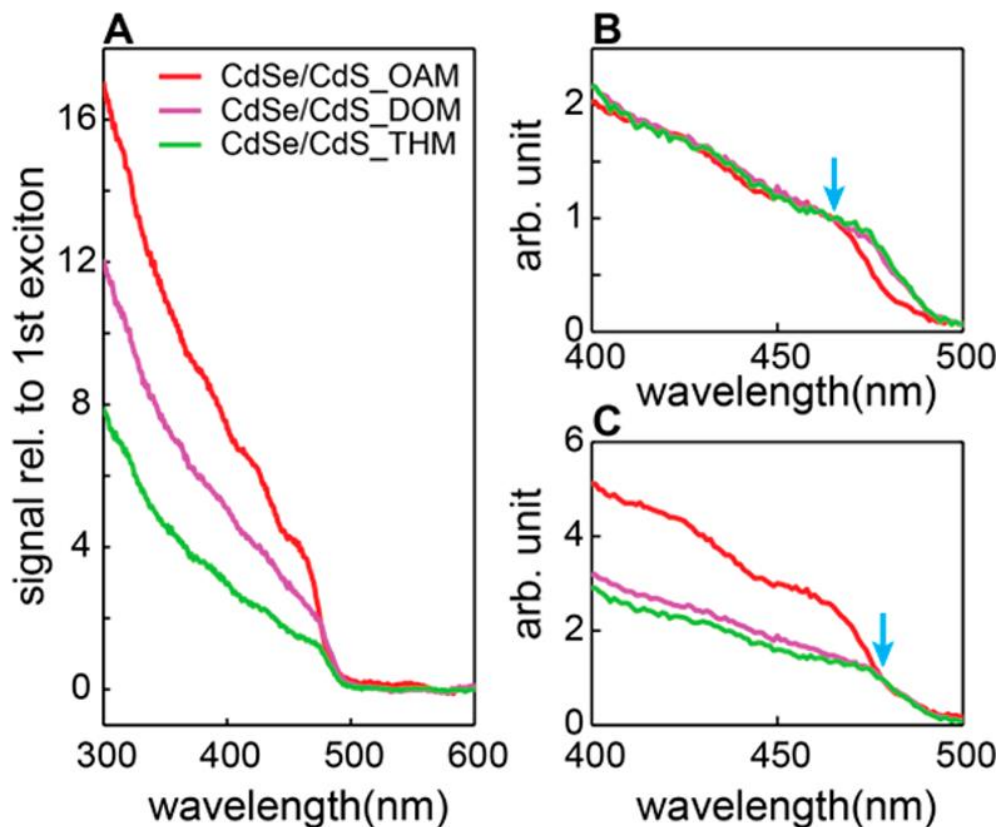
Figure 2.3 (A) Comparison of $(1 - T) - PLE$ for 600 nm emission for CdSe/CdS core/shell particles grown in the three amines. (B) Curves in (A) normalized at the first peak of sample **CdSe/CdS_OAM** (blue arrow). (C) Curves in (A) normalized close to the signal onset (blue arrow). Copyright 2015 American Chemical Society.

2.4 Amine influence on particle photoluminescence lifetime

We recorded time-resolved PL traces of aliquots drawn over the course of shell growth in the three amine solvents to characterize the average decay rate and decay rate dispersion in the samples. The amine solvent can act as a ligand for the QD surface and as such could inhibit the binding of shell growth precursors, in particular Cd(oleate)$_2$. We have shown previously that association of oleylamine to the surface of purified CdSe/CdS core/shell QDs increases the ensemble QY, increases the average PL lifetime, and

16

decreases rate dispersion.[39] Comparison of the PL decay traces of CdSe QDs and core/shell QDs in the presence of the three amine solvents could thus serve as a proxy measurement for ligand interactions with the QD surface that influence growth. Additionally, as shell growth proceeds, the solvent may modulate polydispersity and/or the formation of crystal defects during shell growth, which would affect radiative and nonradiative decay rates, respectively.
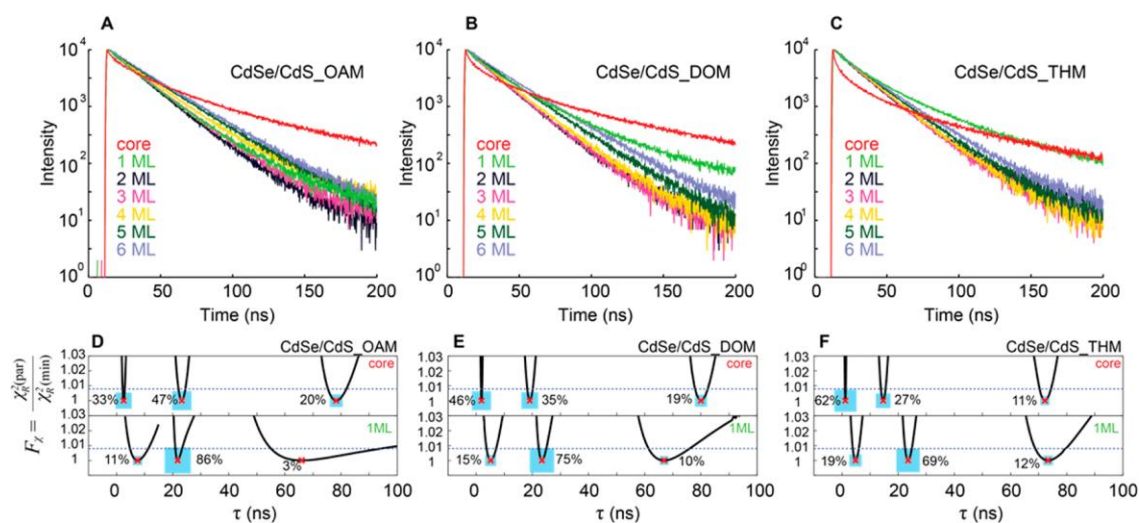

Figure 2.4 (A−C) Time-resolved PL monitored over the course of CdSe/CdS core/shell QDs growth in three amines. (D−F) Distribution of lifetimes for cores (top) and core/shell particles with 1 ML equivalent shell (bottom) in three amines, as well as the relative amplitudes for each exponential component (blue squares, area represents wt A_i for the ith component). Support plane analysis is applied to determine the uncertainties in the lifetimes of each fit component. Blue dashed line indicates 90% confidence limit for F statistic. Copyright 2015 American Chemical Society.

Figure 2.4A−C shows the PL decays for each sample just prior to introduction of shell precursors and after each successive complete ML equivalent of growth. To isolate the influence of the amine solvents as ligands on the luminescence kinetics, we can focus on the traces for the cores (red traces). After being heated in the shell growth solvent, but prior to introduction of shell precursors, the amplitude average lifetime was greatest for oleylamine: $\tau_{avg\_OAM} = 27.7$ ns $> \tau_{avg\_DOM} = 22.7$ ns $> \tau_{avg\_THM} = 12.6$ ns. All samples

17

showed multiexponential decays. For quantitative analysis of lifetimes and decay rate dispersion, experimental curves were fit with a sum of exponential components reconvoluted with the instrument response function. At least three exponential components were required for a reasonably good fit ($\chi_R^2 < 1.5$). In each case, three component fits returned an intermediate lifetime component (τ_2) on the order of the radiative lifetime, a short-lifetime component (τ_1), and a long lifetime component (τ_3) that is likely associated with a trapping/detrapping mechanism.[50] To characterize the uncertainty in the lifetime values, we examined how χ_R^2 changes when one parameter is varied and the others are reoptimized, also called support plane analysis[51] (**Figure 2.4D−F**). For each decay, we found the lifetimes to be well separated from each other at a 90% confidence limit. The shorter average lifetimes for dioctylamine and trihexylamine samples are driven both by a shift in τ_1 and τ_2 to smaller values and by a shift in amplitude toward the short-lifetime component (**Figure 2.4D−F**, top), indicative of a larger fraction of the ensemble residing in a state with a large nonradiative decay rate. These observations are consistent with a stronger binding interaction of oleylamine with the QD surface, resulting in better electronic passivation of the QD surface, but also potentially interfering with precursor conversion during shell growth.

For further core/shell growth in all three amines, the relative amplitude for short-lifetime (wt A_1) and long-lifetime (wt A_3) components continuously decreased, while the relative amplitude for the intermediate component (wt A_2) increased greatly only after 1 ML (**Figure 2.4D−F**, bottom). For CdSe/CdS_OAM, the short lifetime component was completely eliminated after 2 ML of shell. The amplitude average lifetimes kept increasing from 20.76 to 27.48 ns (and only require two exponential components to fit the

decay). For CdSe/CdS_DOM, the short lifetime component disappeared after 4 ML of shell, with the amplitude average lifetimes increasing from 19.36 to 26.53 ns. However, for CdSe/CdS_THM, the short lifetime component existed even after 6 ML of shell growth, and the amplitude average lifetimes remained at 20−23 ns over the course of the growth. This difference in average lifetime at the conclusion of 6 ML is primarily associated with the larger amplitude and smaller lifetime value of the τ_1 component; the value of τ_2 is nearly identical across the three samples.

Shell growth introduces an electronic barrier (at least for holes) between the core and surface. In our shell growth method, TOP is a component of the shell precursor solution; TOP binds exothermically to the QD surface and is known to strongly regenerate QY in purified samples.[39] Nonetheless, the difference in average lifetime and rate dispersion among the three amine solvents persists through 6 ML of shell growth, suggesting that effects of ligand occupation of the surface on precursor conversion may likewise persist through the course of shell growth in the presence of TOP.

2.5   STEM images of core/shell nanoparticles

Figure 2.5 shows the STEM images and radius distribution histograms for CdSe cores as well as the three core/shell products. The radius histograms are determined by analysis of STEM images of the same magnification at 6−7 randomly selected regions; N is the number of particles analyzed. In comparing STEM images of **Figure 2.5A-D** and the radius histograms of **Figure 2.5E−H**, the differences in particle sizes and distributions are clearly displayed. We characterize the average radius and peak radius for particles; the average radius is obtained directly from the distribution (including small

19

particles), while the peak radius is the center of a Gaussian fit (red curve, **Figure 2.5E−H**) to the distribution and represents a characteristic radius for core/shell particles in the sample.
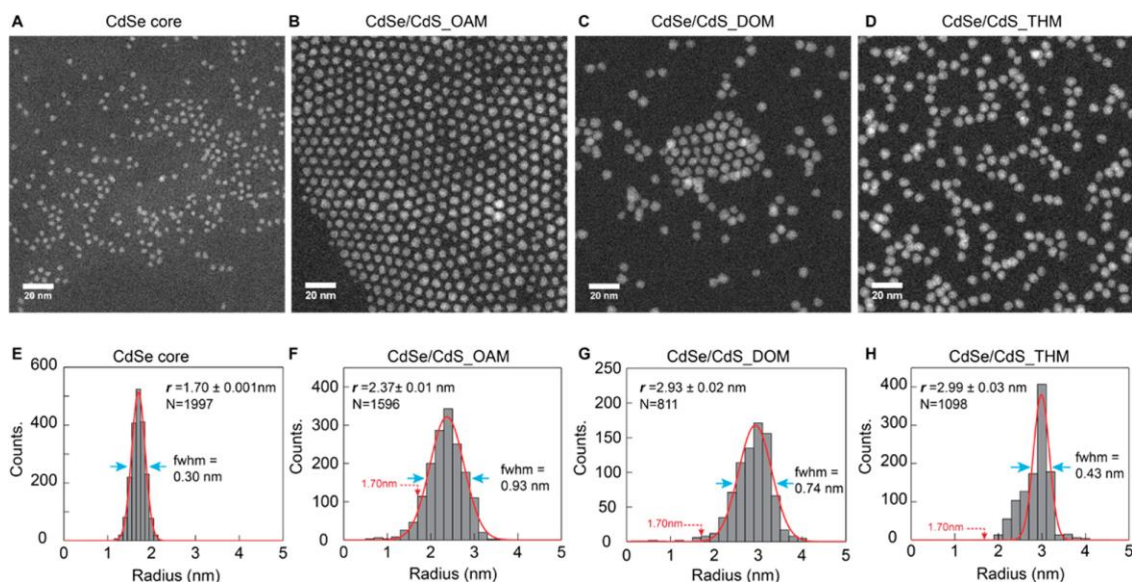

Figure 2.5 STEM images and radius histograms for CdSe cores (A,E) and core/shell samples **CdSe/CdS_OAM** (B,F), **CdSe/CdS_DOM** (C,G), and **CdSe/CdS_THM** (D,H). The histograms are fitted by Gaussian functions (red curves, E−H) to determine the peak radius; the fwhm is indicated by blue arrows. Copyright 2015 American Chemical Society.

A majority of particles in the core/shell samples showed a radius larger than that of the cores and commensurate with shell growth; however, CdSe/CdS_DOM (**Figure 2.5C**) and CdSe/CdS_THM (**Figure 2.5D**) showed larger average and peak radius as compared to CdSe/CdS_OAM (**Figure 2.5B**). Additionally, both CdSe/CdS_DOM and CdSe/CdS_THM showed narrower size distributions and showed particles with more uniform shapes. Inspection of the STEM images reveals the presence of a significant number of particles smaller than the CdSe cores in CdSe/CdS_OAM. Although the STEM images cannot clearly resolve CdS from CdSe, we can assign the smallest particles as a CdS nanoparticle side product. These small particles contribute to the

20

smaller average radius in this sample. The peak radius primarily describes the core/shell product; it is the smallest in CdSe/CdS_OAM as well, indicative of thinner CdS shells due to loss of material to the side product. At the same time, the distribution of radius for CdSe/CdS_OAM (fwhm = 0.93 nm) is broader than that for CdSe/CdS_DOM (fwhm = 0.74 nm) and CdSe/CdS_THM (fwhm = 0.43 nm). Core/shell particles growing in trihexylamine maintained a very narrow size distribution, nearly as good as the cores (fwhm = 0.30 nm), although a small fraction of particles with radius down to 2.5 nm (**Figure 2.5H**) remained present.

The STEM results confirm that the more highly substituted amines dioctylamine and especially trihexylamine were effective in suppressing the nucleation of small particles during shell growth, and the observation of small particles in the CdSe/ CdS_OAM and CdSe/CdS_DOM samples corroborates the assignment of the blue PL peaks as radiative recombination from CdS nanoparticles. Examination of the shapes of nanocrystals in the three core/shell samples appears to show greater roundness in CdSe/CdS_DOM and CdSe/CdS_THM, suggesting that conditions that suppress nucleation also help to enforce isotropic shell growth. High magnification STEM images in **Figure 2.6** reveals the greater roundness observed in highly substituted amines syntheses.
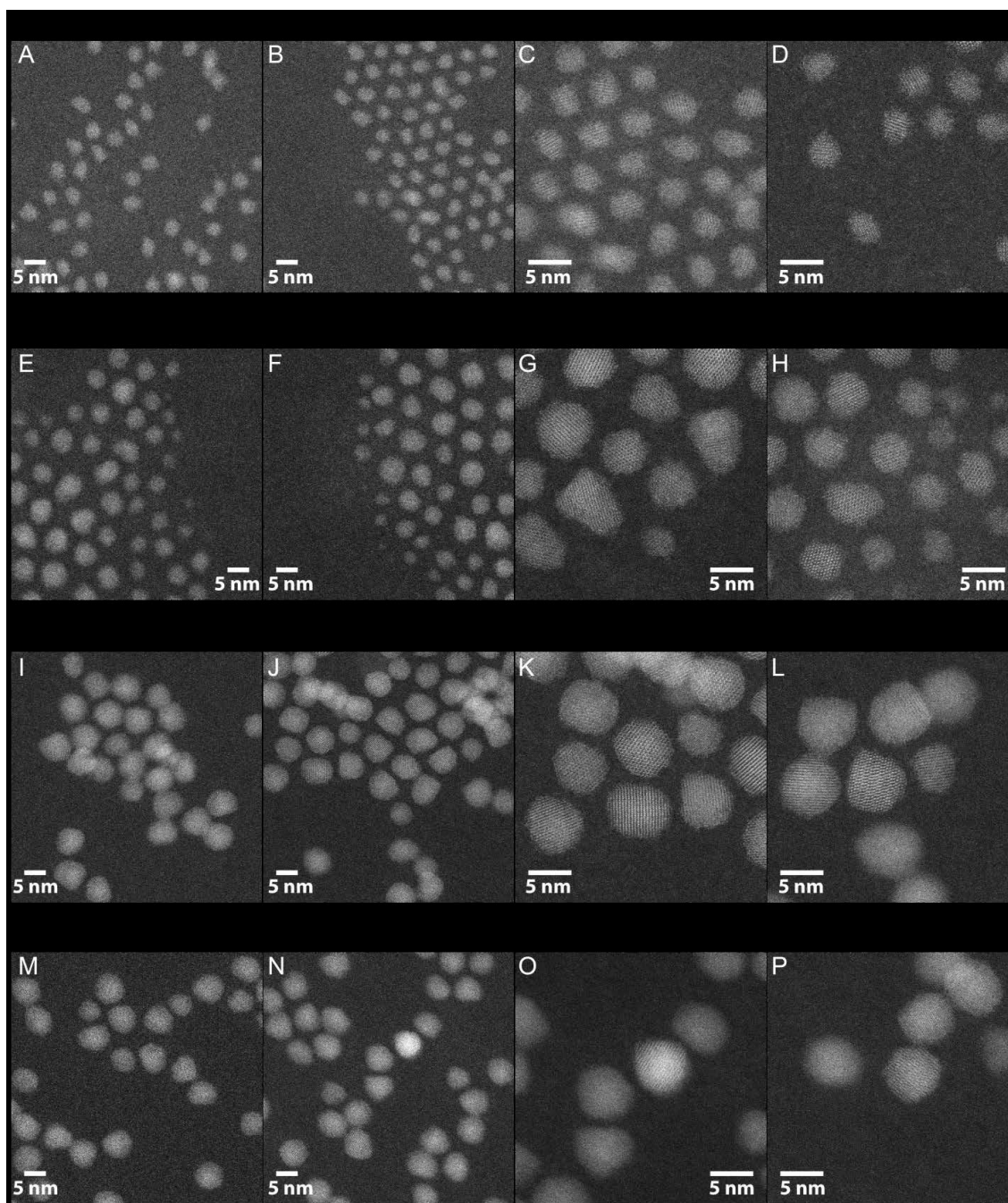
Figure 2.6 High magnification STEM images for CdSe cores, and for **CdSe/CdS_OAM**, **CdSe/CdS_DOM**, and **CdSe/CdS_THM**. Panels E,F reveal particles in **CdSe/CdS_OAM** with sizes smaller than is characteristic of the CdSe cores (A,B). Higher magnification images (G,H and below) reveal un-spherical shapes. Compared with **CdSe/CdS_OAM, CdSe/CdS_DOM** and **CdSe/CdS_THM** particles are more uniform in shape have narrower size distributions. Copyright 2015 American Chemical Society.

2.6 Conclusion

We have confirmed that replacing oleylamine with a secondary amine, dioctylamine, suppresses nucleation and improves core/shell growth, and we have shown that moving to a tertiary amine, trihexylamine, is even more effective. The use of time-resolved PL has shown that more highly substituted amines bind less strongly to the surface of CdSe QDs, permitting a greater precursor conversion. We can also conclude that oleylamine effectively competes with the precursor $Cd(oleate)_2$ for occupation of nanocrystal surface sites, leading to a significant amount of cross-reaction and nucleation of CdS particles during CdS shell growth by SILAR.

2.7 Experimental Section

Materials: The following chemicals were used as received. Cadmium oxide (CdO; 99.999%), trioctylphosphine (TOP; 97%), and trioctylphosphine oxide (TOPO; 99%) were purchased from Strem Chemicals. Oleic acid (OA; 99%), 1-octadecene (ODE; 90% technical grade), 1-tetradecylphosphonic acid (TDPA; 98%), and Se (99.999%) were purchased from Alfa Aesar. Di-n-octylamine, 98% (LOT:10178704) and Tri-n-hexylamine, 97% (LOT:G18S028) are purchased from Alfa Aesar. Decylamine (95%) was purchased from Sigma Aldrich. Oleylamine (80-90%) and bis(trimethylsilyl) sulfide ($(TMS)_2S$; 95%) were purchased from Acros Organics. 200 proof ethyl alcohol (ethanol) was obtained from Decon Laboratories, Inc. Acetone (99.9%) was purchased from VWR. Ethanol (99.9%) was purchased from Fisher Scientific. TOPSe (2.2 M) was prepared by dissolving Se in TOP. A stock solution of $Cd(oleate)_2$ (0.2 M) in ODE was prepared by heating CdO in ODE with 2.2 equivalents of oleic acid at 260 °C under nitrogen,

23

followed by degassing under vacuum at 100 °C for 20 min. The sulfur precursor was 0.1 M solution of (TMS)$_2$S dissolved in TOP. Nanocrystal core and shell growth was carried out under nitrogen (N$_2$) using Schlenk line techniques; air-sensitive reagents were prepared in a nitrogen filled glovebox.

Optical Spectroscopy: The optical absorption spectrum was recorded using a Thermo Scientific Evolution Array UV−visible spectrophotometer with hexane as the solvent as well as the blank in a 1 cm path quartz cuvette. Routine emission spectra were recorded by an Ocean Optics USB 4000 spectrometer under ∼365 nm excitation.

Synthesis of CdSe Cores: A hot-injection technique was applied for synthesis of CdSe nanocrystals (NCs) cores.[52] For a representative synthetic route, CdO (0.12 g) was heated with TDPA (0.5500 g) at 330°C in a solvent TOP (6 ml) and TOPO (6 g) under nitrogen flow until the solution became colorless. Following removal of evolved H$_2$O under vacuum at 130°C, the solution was heated again to 360°C under nitrogen. As-prepared TOPSe (1.3 mL) was injected rapidly into the reaction pot, which was immediately allowed to cool down to room temperature and stored as a yellow waxy solid. The Cd:TDPA:Se molar ratio is 1:2:3. The core radius was estimated by a calibration curve[52,53] describing the radius as a function of the position of the lowest-energy absorption peak. One batch of cores provided sufficient material for several core/shell growth experiments; all core/shell particles were made based on the CdSe QD cores taken from the same batch.

Synthesis of Core/Shell Nanoparticles in Different Amines: The method for CdSe/CdS core/shell particle growth was modified from our previous work.[34,52] The difference was switching different types of amines (oleylamine, dioctylamine,

24

trihexylamine) in the solvent mixture. The Cd precursor was prepared by diluting Cd(oleate)$_2$ stock solution in a solvent of 50:50 ODE and TOP with two equivalents of the same amine in the solvent mixture (vs. Cd) added to yield a Cd concentration of 0.1 M.; The sulfur precursor was 0.1 M solution of (TMS)$_2$S dissolved in TOP. The CdS shell was grown by alternatively introducing Cd & sulfur precursors into the reaction flask, 1 ML eq. of precursors added per cycle, and forming 6 ML of CdS shell in total after six cycles. Reaction progress was monitored by periodically withdrawing a small aliquot of a measured volume (typically 50 μL) from the reaction flask and diluting it in hexanes at room temperature; these aliquots were analyzed for UV-vis absorption and fluorescence emission in hexanes solution.

Time-Resolved Photoluminescence Measurement: The PL decays of QDs in hexane were collected in front-face mode with 1 cm quartz cuvette in a lifetime spectrometer (Edinburgh Mini-τ) equipped with a 368 nm picosecond-pulsed-light-emitting diode. A stirring stage was set under the Mini-τ, and a mini stir bar was placed in the cuvette to stir the QD solution to avoid accumulation of photoproducts during the measurement. The instrument response function (IRF) is recorded using Rayleigh scattering of pure water.

Scanning Transmission Electron Microscopy Imaging: After purification, the CdSe or CdSe/CdS core/shell QDs were brought into hexane to form a dilute solution (1.1 μM), one drop of the solution was drop-casted on a clean TEM grid (400 mesh Cu grid with ultrathin carbon support film, Type-A, Ted Pella, Inc.) and pumped dry under vacuum for 2 hours. The STEM samples were imaged by JEOL 2100F 200 kV FEG-STEM/TEM equipped with a CEOS CS corrector on the illumination system. Prior to

25

high magnification observation, a large specimen area was pre-irradiated with electrons for 10 minutes to polymerize surface hydrocarbons and therefore prevent their diffusion to the focused probe. High angle annular dark-field (HAADF) STEM images were acquired on a Fischione Model 3000 HAADF. A pixel dwell time of 16 µs was chosen.

CHAPTER 3

MAGNETIC NANOPARTICLE TARGETING

3.1 Introduction

Nanomaterials for biomedical use have been increasingly explored in recent years, due to their promise for superior therapeutic results. Specifically, magnetic nanoparticles have been explored in a medical context for numerous applications, including for magnetic drug targeting in cancerous tumors.[17] Yet despite hundreds of thousands of Americans suffering myocardial infarctions (heart attacks) every year, the focus of these research efforts has largely been placed on other medical issues.

By concentrating on effective cardiovascular delivery methods, improved treatment can be achieved for those afflicted with cardiovascular maladies. Therapeutic agents have been identified for these conditions, but adverse effects and inability to reach effective local dosage has resulted in a lack of options for treatment. The creation of nanoparticles that enable the binding of pharmacological agents to the surface, coupled with retention of the magnetic properties, would be a boon to the current issue plaguing potential treatments. Medicine-laden magnetic nanoparticles could be administered intravenously, concentrated in the effected region via a local magnetic field, allowing the payload to be released and creating an area of increased dosage, thereby reducing the amount of free drug required to have a beneficial effect while limiting the adverse effects on the patient.

The Benicewicz group has previously developed a method to utilizing reversible addition fragmentation chain transfer (RAFT) polymerization of methacrylic acid on the surface of Fe_3O_4/SiO_2 nanoparticles.[54] Benzylpenicillin, **Figure 3.1**, was then physically bound to the surface of the grafted nanoparticles and disk diffusion assays demonstrated an increased anti-bacterial response, due to an increased localized concentration of benzylpenicillin. Using the surface preparation established the aforementioned work, we explored the binding of a representative medicinal compound to nanoparticles.

In this work, we demonstrated that capture of magnetite nanoparticles as prepared by the Benicewicz group (**Figure 3.2**) is possible in vitro under biological flow conditions. As the nanoparticles have a shell and additional ligands on the surface, it is important to verify that the particles retained their superparamagnetic nature and that a relatively low magnetic strength was sufficient for capture of the particles. Exploration of the adsorption of a representative drug (**Figure 3.3**) compound to the nanoparticle in buffered solutions, as well as DI H_2O, was performed and monitored using UV-visible absorption spectroscopy.
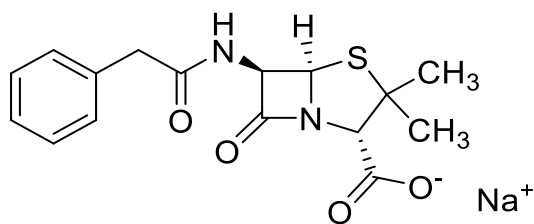

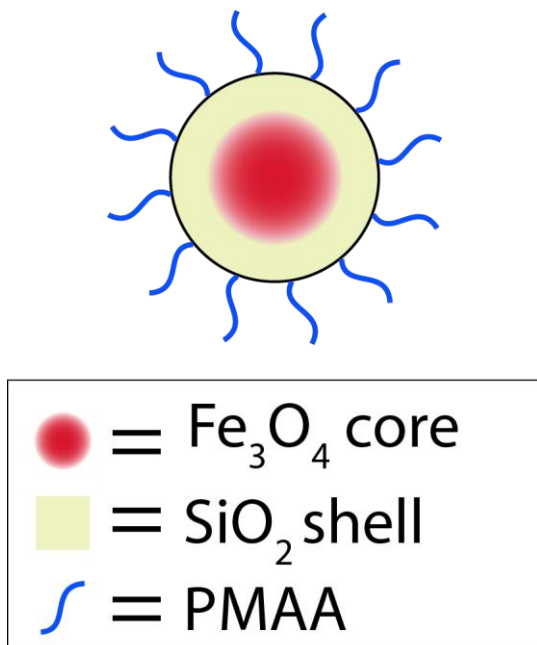**Figure 3.1** Chemical structure of benzylpenicillin.

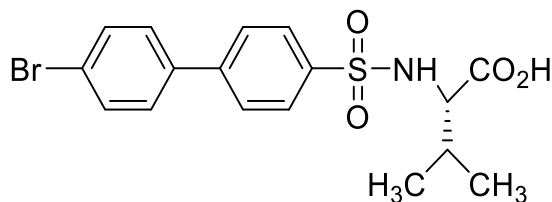**Figure 3.2** Fe$_3$O$_4$/SiO$_2$/PMAA nanoparticle structure

Figure 3.3 Chemical structure of drug compound PD166793.

3.2 In Vitro Magnetite Particle Capture

Preliminary experiments have been performed on magnetite (Fe$_3$O$_4$) nanoparticles with a shell of SiO$_2$ and grafted with poly(methacrylic acid) (PMAA). To test initial feasibility of nanoparticle capture by a magnetic field, a magnet was placed on the surface of plastic tubing and a solution of nanoparticles in water was flowed through the tube using an automated syringe pump, a method which has previously been used to test the capture of magnetic particles.[32] In order to determine the percentage of total particles

29

captured by the magnet, an amount of solution was first flowed with no magnet being present and the solution was captured for analysis. The same amount of solution was again flowed, but with a magnet placed against the surface of the tube to capture the nanoparticles, and the solution was captured. The magnet was then removed from the surface of the tube and the final portion was flowed and captured, which should contain the initial concentration of particles in the solution in addition to the particles that had previously been captured in the tube. The captured aliquots were analyzed using UV/Vis spectroscopy.
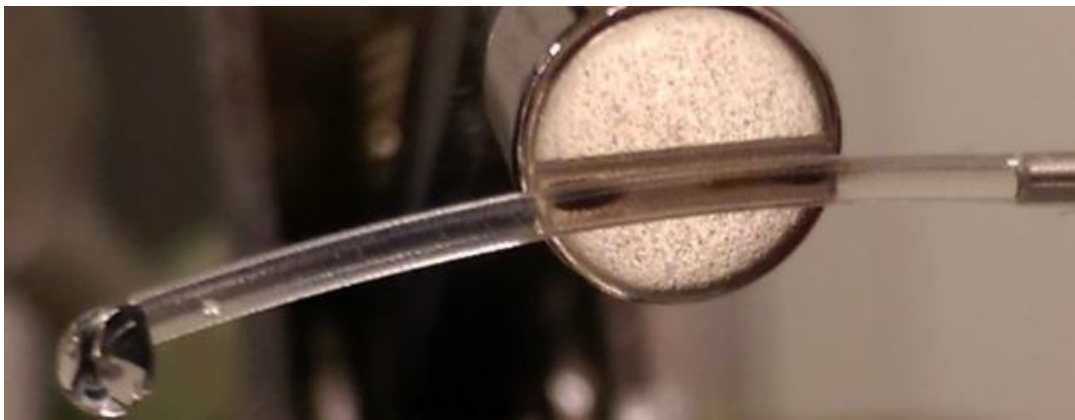

Figure 3.4 Fe_3O_4/SiO_2/PMAA SPIONs captured in 0.6 mm inner diameter tube at 4 mm/sec flow rate.
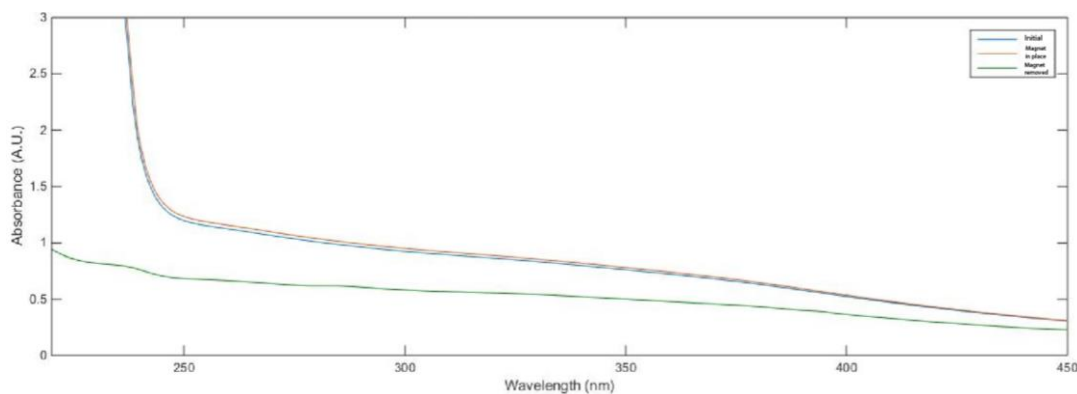

Figure 3.5 Absorption spectrum of 4 mm/s flow rate in 0.6 mm inner diameter tube.

Figure 3.6 $Fe_3O_4/SiO_2/PMAA$ SPIONs captured in 0.6 mm inner diameter tube at 20 mm/sec flow rate.
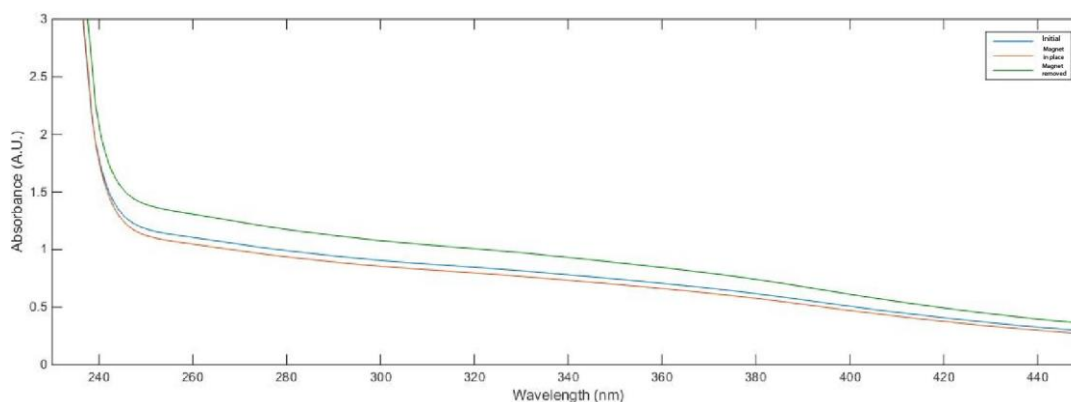

Figure 3.7 Absorption spectrum of 20 mm/s flow rate in 0.6 mm inner diameter tube.

Analysis of the UV-Vis spectrum (**Figure 3.5**) for the 4 mm/s at 50 µg iron oxide/mL trial revealed a 17.7% increase in signal at 350 nm between the first run of the solution with no magnet present and the third run. The increase was expected due to the additional particles that should be present in the solution. However, for the 20 mm/s flow rate at 50 µg of iron oxide/mL, the spectrum (**Figure 3.7**) showed a decrease from the initial run to the third run, even though captured particles were visibly evident (**Figures 3.4 and 3.6**) in the tube during the experiment. These inconsistent results indicate that further verification of sources of error is necessary.

31

3.3 Binding to SiO$_2$ Nanoparticles

In order to test the feasibility of binding for the representative MMP inhibitor, PD166793, analogous silica nanoparticles coated with PMAA were used in place of magnetic nanoparticles. The binding trials were run in various solutions to explore the effect of pH and salt concentration on the ability to bind. Detailed procedures are described in the experimental section. **Figure 3.8** and **Figure 3.9** show that the drug does not bind in 50% PBS or acetate buffers, respectively. **Figure 3.10** shows peaks after centrifugation in DI water that appear around 273 nm, indicating that drug compound is present in the retentate and presumably bound to the silica nanoparticles.

By varying the nominal drug concentration, as shown in **Figure 3.11**, we were able to examine if the amount of drug was limiting the signal being seen in the absorption spectra, as well as if drug binding would scale as the amount of available drug increased while holding the concentration of particles consistent. **Figure 3.12** has the same variation in drug concentration, but double the nominal nanoparticle concentration. As the drug concentration is increased, the ratio of the amount of bound drug vs. the total amount of drug available increases indicating that the drug appears to bind more effectively at higher concentrations. However, the bound drug per nominal nanoparticle seems to scale linearly with respect to drug concentration.
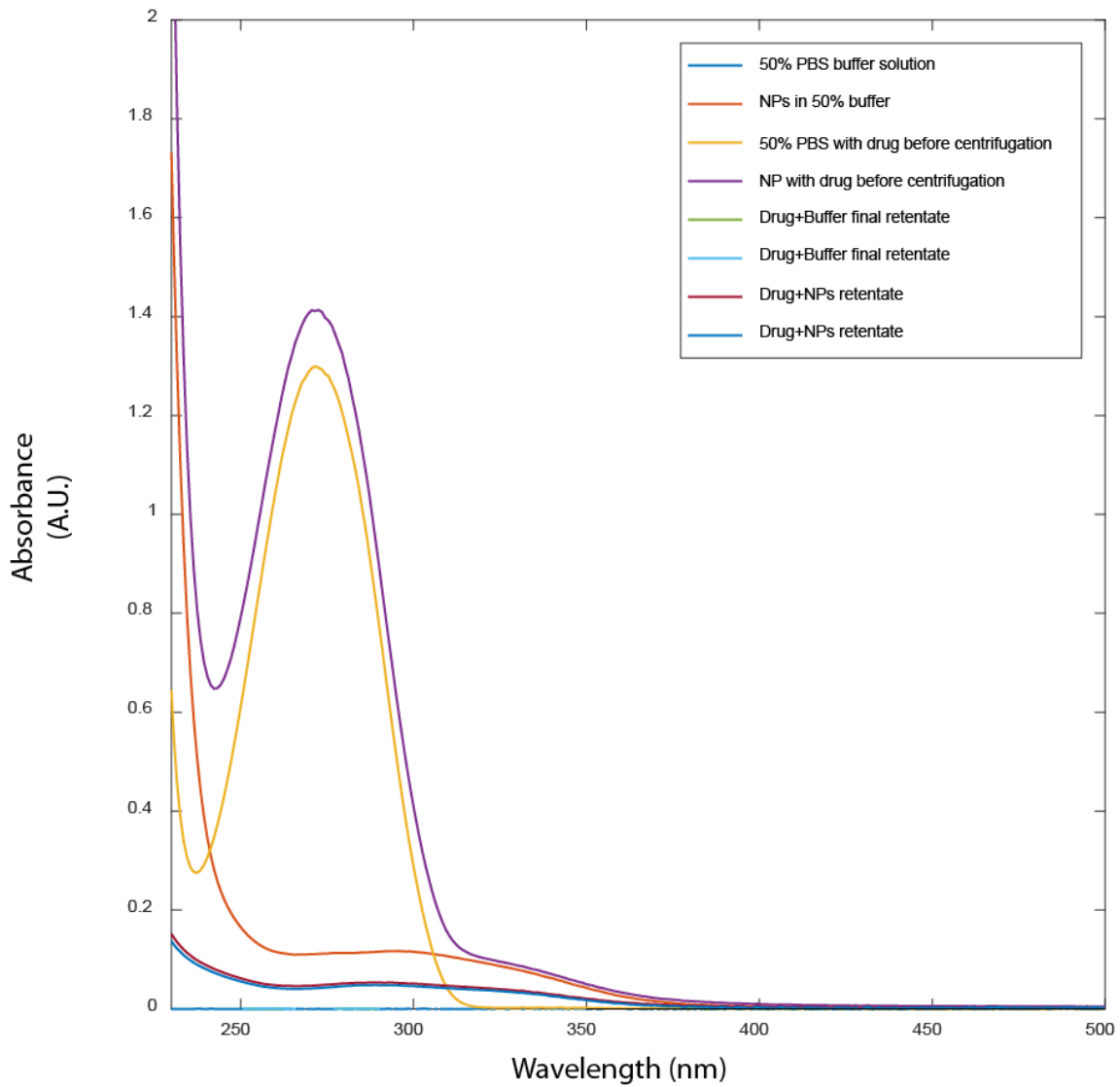
32

Figure 3.8 Absorption spectrum of 2.5 mg/mL Si NP with 12.5 µg/mL drug in PBS buffer.

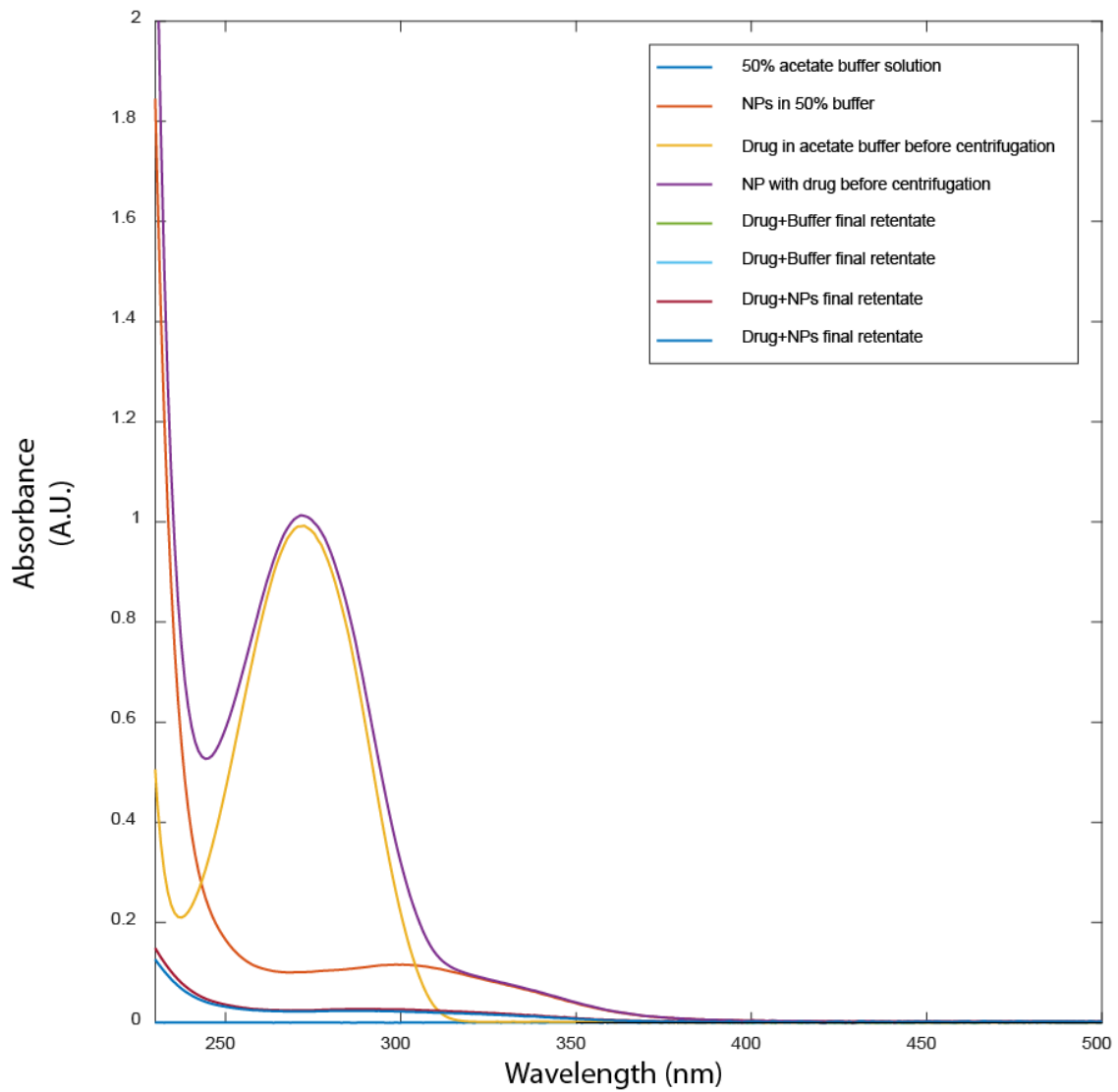**Figure 3.9** Absorption spectrum of 2.5 mg/mL Si NP with 12.5 µg/mL drug in acetate buffer.
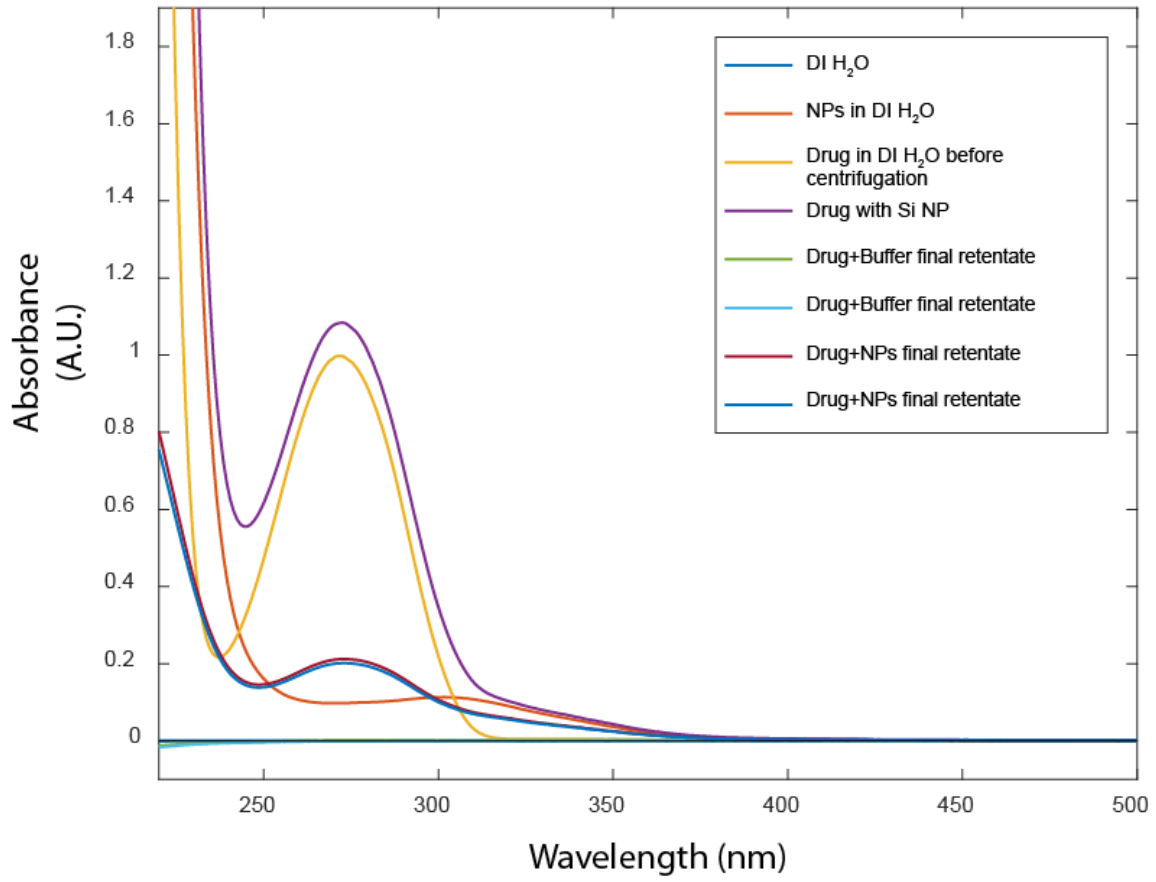
Figure 3.10 Absorption spectrum of 2.5 mg/mL Si NP with 12.5 µg/mL drug in DI H₂O.
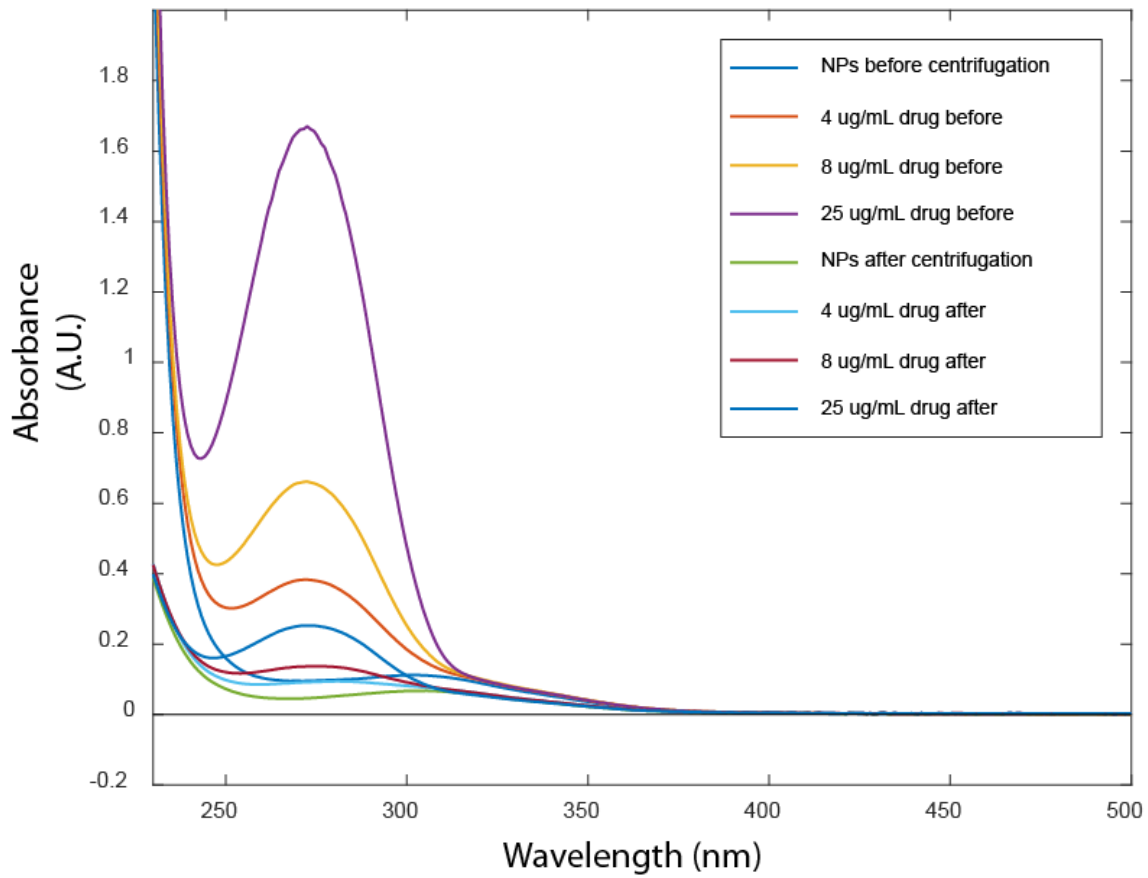
Figure 3.11 Absorption spectrum of 2.5 mg/mL Si NP with varied drug concentration in DI H$_2$O.
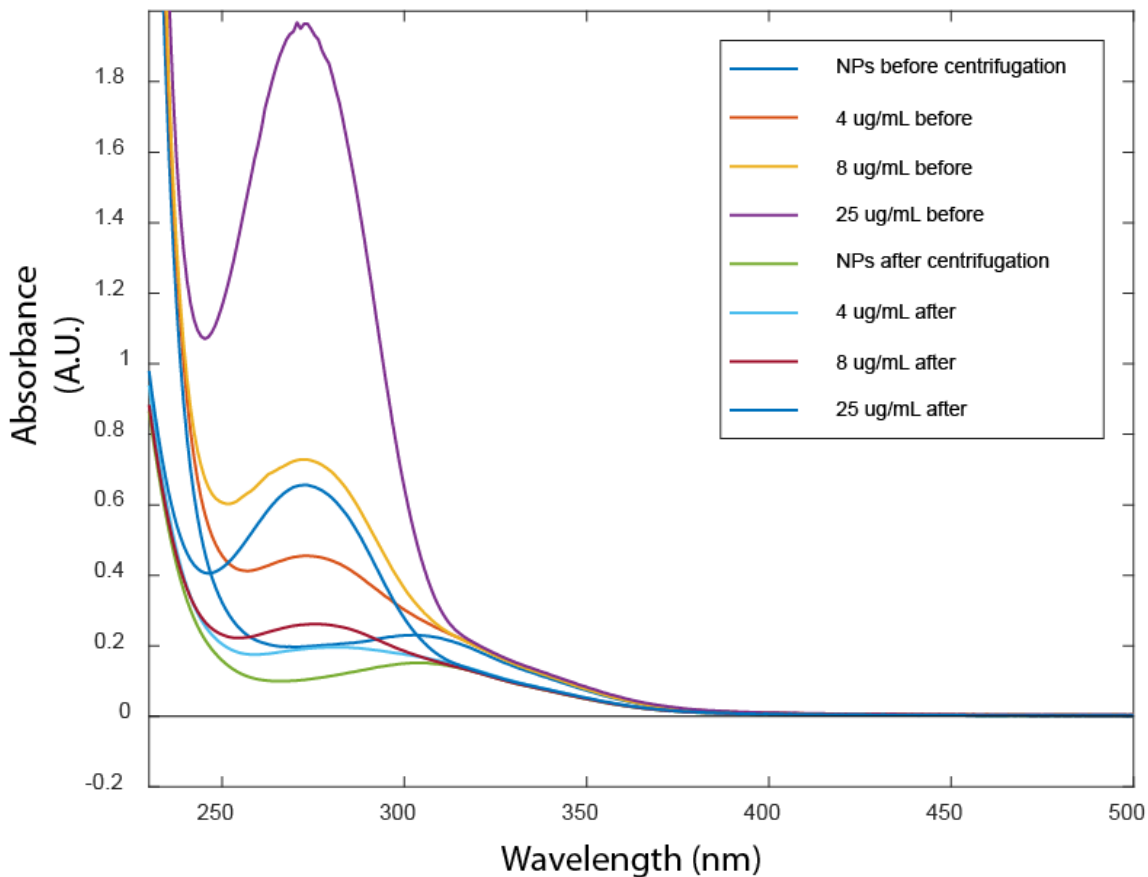
Figure 3.12 Absorption spectrum of 5 mg/mL Si NP with varied drug concentration in DI H₂O.

We have seen that the drug compound PD166793 is fluorescent, as shown in **Figure 3.13**. The ability to use fluorescent anisotropy would allow us to better observe the extent of drug binding to the nanoparticles, while providing insight into the binding kinetics occurring, as it could indicate a dynamic binding equilibrium in which the drug dissociates within the timescale of the centrifugation, when the free drug concentration is reduced. By binding to the nanoparticles, the anisotropy value should increase due to the impeded rotation of the particle in situ.
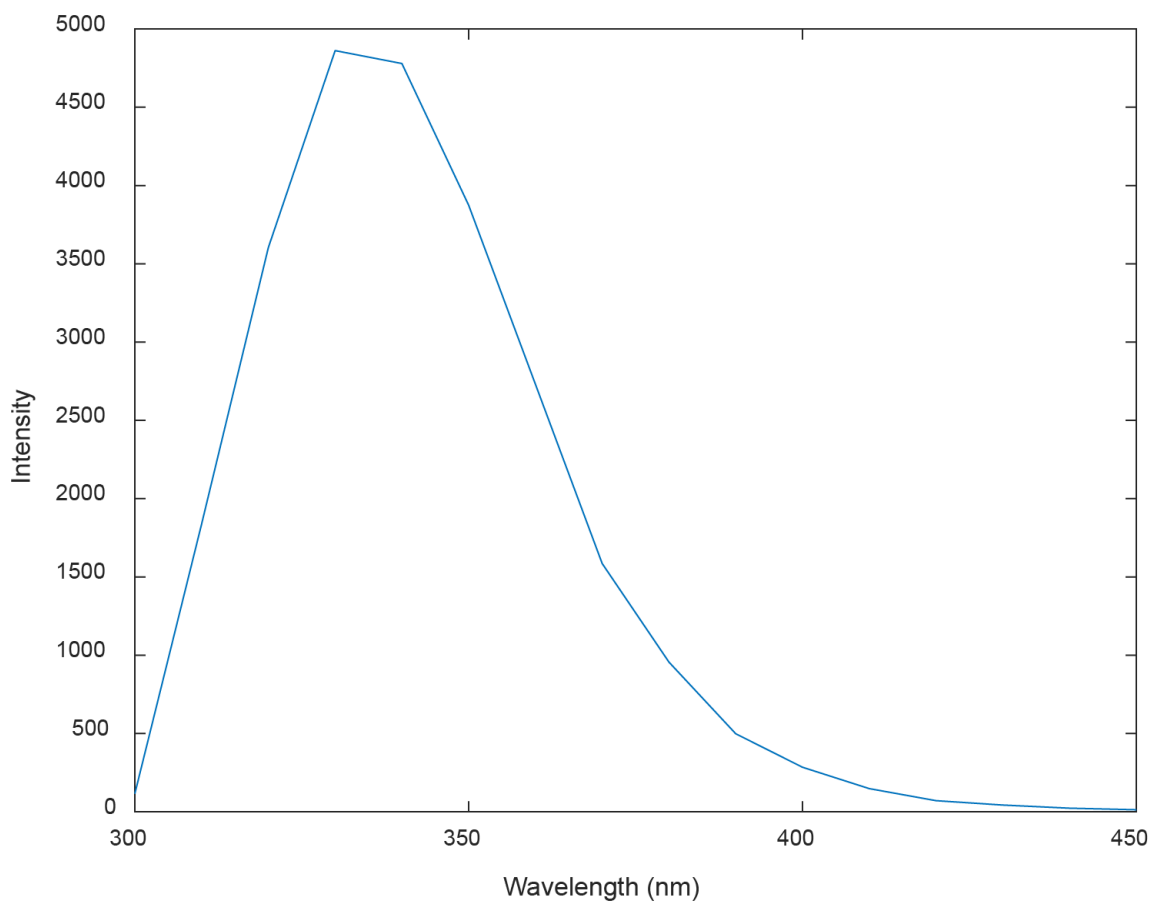
Figure 3.13 Fluorescence spectrum of PD166793 with peak at 330 nm.

3.4 Conclusion

Through flow field fractionation, we have shown that we are able to capture the nanoparticles in conditions similar to biological applications. While the capture was visibly evident within the tubes, a technique other than absorption spectroscopy might prove beneficial to accurately measure the amount captured. The representative drug compound binds to the PMAA SiO_2 nanoparticles in DI H_2O, as seen in UV-Vis absorption spectra. However, it appears that the addition of salts in the form of buffer solution prevents the drug from binding. In order to better understand the binding kinetics of the drug to nanoparticle, fluorescence anisotropy measurements could be utilized.

3.5 Experimental Section

Materials: The following chemicals were used as received. PD166793 was purchased from Sigma-Aldrich. Dimethyl sulfoxide (DMSO) was purchased from VWR.

Preparation of Fe_3O_4/SiO_2 Nanoparticles: The Fe_3O_4/SiO_2 nanoparticles were synthesized by students from Dr. Brian Benicewicz's group at University of South Carolina. The synthesis method has been previously published.[54] The nanoparticles were received with dimethylformamide (DMF) as the solvent. In order to mimic biological conditions, they were transferred into water as follows: An amount of original solution was taken and placed in a 7 mL vial. A magnet was then placed near the vial wall and left to sit for several hours. After the nanoparticles collected near the magnet and the rest of the solution had turned clear, the magnet was held in place and the DMF was poured off. The particles were then redissolved with water to give the desired concentration.

Magnetic Capture: The necessary amount of solution was taken into a 20 mL syringe and the needle was switched to a blunted needle with tubing 20 mm in length and 0.64 mm in diameter. Excess air was expelled from the syringe, needle, and tube and the syringe set-up was placed in the programmable syringe pump (New Era Pump Systems Inc.). The previously made program, based on the desired flow rate, was run. Three aliquots were collected for each trial: 1) Initial solution with no magnet in place. 2) Initial solution with NdFeB magnet (grade N52, 5/16" dia. x 1/4" thick, surface field: 6275 Gauss) in place for particle capture. 3) No magnet in place, resulting in initial solution and additional captured particles in aliquot. Each aliquot then underwent UV-Vis

characterization using a Thermo Scientific Evolution Array UV−visible spectrophotometer as well as a blank in a 1 cm path quartz cuvette.

Drug Binding to SiO₂ Nanoparticles: The PMAA grafted SiO_2 nanoparticles were synthesized by Yang Zheng from Dr. Brian Benicewicz's group at University of South Carolina. Stock solutions (100 mg/mL) of the drug compound (PD166793) were prepared in dimethyl sulfoxide (DMSO). To complex the drug to the nanoparticles, the drug compound was added to a vial containing nanoparticles and either buffer or DI H_2O and stirred for several hours. Control trials were performed by omitting the nanoparticles from the solution. Each trial had the same centrifugation process: 1) 2 mL of prepared drug solution added to Amicon Ultra-4 centrifugal filter tubes 2) 2 mL of corresponding solvent added to tubes 3) Centrifuge at 6236 RPM for 5 minutes 4) Collected eluent and dilute retentate to 4 mL 5) Step 3 was repeated, the eluent was collected, and the complexed samples were extracted from the centrifugal filters and diluted (usually 2 mL) into the corresponding solvent at room temperature. The optical absorption spectra were recorded using a Thermo Scientific Evolution Array UV−visible spectrophotometer.

40

REFERENCES

(1) Rogach, A. L. E. *Semiconductor Nanocrystal Quantum Dots*; Springer-Verlag Wien: Wien, 2008.

(2) Bae, W. K.; Brovelli, S.; Klimov, V. I. Spectroscopic Insights into the Performance of Quantum Dot Light-Emitting Diodes. *MRS Bull.* **2013**, *38*, 721–730.

(3) Talapin, D. V.; Steckel, J. Quantum Dot Light-Emitting Devices. *MRS Bulletin* **2013**, *38*, 685–691.

(4) Wu, X.; Liu, H.; Liu, J.; Haley, K. N.; Treadway, J. A.; Larson, J. P.; Ge, N.; Peale, F.; Bruchez, M. P. Immunofluorescent Labeling of Cancer Marker Her2 and Other Cellular Targets with Semiconductor Quantum Dots. *Nat Biotech* **2003**, *21*, 41–46.

(5) Medintz, I. L.; Uyeda, H. T.; Goldman, E. R.; Mattoussi, H. Quantum Dot Bioconjugates for Imaging, Labelling and Sensing. *Nat Mater* **2005**, *4*, 435–446.

(6) Murray, C. B.; Norris, D. J.; Bawendi, M. G. Synthesis and Characterization of Nearly Monodisperse CdE (E = Sulfur, Selenium, Tellurium) Semiconductor Nanocrystallites. *J. Am. Chem. Soc.* **1993**, *115*, 8706–8715.

(7) Park, Y.-S.; Malko, A. V.; Vela, J.; Chen, Y.; Ghosh, Y.; García-Santamaría, F.; Hollingsworth, J. A.; Klimov, V. I.; Htoon, H. Near-Unity Quantum Yields of Biexciton Emission from CdSe/CdS Nanocrystals Measured Using Single-Particle Spectroscopy. *Phys. Rev. Lett.* **2011**, *106*, 187401.

(8) Murphy, C. J.; Coffer, J. L. Quantum Dots: A Primer. *Applied Spectroscopy* **2002**, *56*, 16A – 27A.

(9) Garrett, M. D.; Bowers, M. J.; McBride, J. R.; Orndorff, R. L.; Pennycook, S. J.; Rosenthal, S. J. Band Edge Dynamics in CdSe Nanocrystals Observed by Ultrafast Fluorescence Upconversion. *J. Phys. Chem. C* **2008**, *112*, 436–442.

(10) García-Santamaría, F.; Chen, Y.; Vela, J.; Schaller, R. D.; Hollingsworth, J. A.; Klimov, V. I. Suppressed Auger Recombination in "Giant" Nanocrystals Boosts Optical Gain Performance. *Nano Lett.* **2009**, *9*, 3482–3488.

(11) Htoon, H.; Malko, A. V.; Bussian, D.; Vela, J.; Chen, Y.; Hollingsworth, J. A.; Klimov, V. I. Highly Emissive Multiexcitons in Steady-State Photoluminescence of Individual "Giant" CdSe/CdS Core/Shell Nanocrystals. *Nano Lett.* **2010**, *10*, 2401–2407.

(12) Keene, J. D.; McBride, J. R.; Orfield, N. J.; Rosenthal, S. J. Elimination of Hole–Surface Overlap in Graded $CdS_xSe_{1–x}$ Nanocrystals Revealed by Ultrafast Fluorescence Upconversion Spectroscopy. *ACS Nano* **2014**, *8*, 10665–10673.

(13) Gong, K.; Kelley, D. F. Lattice Strain Limit for Uniform Shell Deposition in Zincblende CdSe/CdS Quantum Dots. *J. Phys. Chem. Lett.* **2015**, *6*, 1559–1562.

(14) Li, J. J.; Wang, Y. A.; Guo, W.; Keay, J. C.; Mishima, T. D.; Johnson, M. B.; Peng, X. Large-Scale Synthesis of Nearly Monodisperse CdSe/CdS Core/Shell Nanocrystals Using Air-Stable Reagents via Successive Ion Layer Adsorption and Reaction. *J. Am. Chem. Soc.* **2003**, *125*, 12567–12575.

(15) Greytak, A. B.; Allen, P. M.; Liu, W.; Zhao, J.; Young, E. R.; Popović, Z.; Walker, B. J.; Nocera, D. G.; Bawendi, M. G. Alternating Layer Addition Approach to CdSe/CdS Core/shell Quantum Dots with near-Unity Quantum Yield and High on-Time Fractions. *Chem. Sci.* **2012**, *3*, 2028–2034.

(16) Cole, A. J.; Yang, V. C.; David, A. E. Cancer Theranostics: The Rise of Targeted Magnetic Nanoparticles. *Trends Biotechnol* **2011**, *29*, 323–332.

(17) Jain, T. K.; Morales, M. A.; Sahoo, S. K.; Leslie-Pelecky, D. L.; Labhasetwar, V. Iron Oxide Nanoparticles for Sustained Delivery of Anticancer Agents. *Mol. Pharmaceutics* **2005**, *2*, 194–205.

(18) Corot, C.; Robert, P.; Idée, J.-M.; Port, M. Recent Advances in Iron Oxide Nanocrystal Technology for Medical Imaging. *Advanced Drug Delivery Reviews* **2006**, *58*, 1471–1504.

(19) Jordan, A.; Scholz, R.; Wust, P.; Fähling, H.; Felix, R. Magnetic Fluid Hyperthermia (MFH): Cancer Treatment with AC Magnetic Field Induced Excitation of Biocompatible Superparamagnetic Nanoparticles. *Journal of Magnetism and Magnetic Materials* **1999**, *201*, 413–419.

(20) Dobson, J. Magnetic Nanoparticles for Drug Delivery. *Drug Dev. Res.* **2006**, *67*, 55–60.

(21) Pankhurst, Q. A.; Connolly, J.; Jones, S. K.; Dobson, J. Applications of Magnetic Nanoparticles in Biomedicine. *J. Phys. D: Appl. Phys.* **2003**, *36*, R167.

(22) Liong, M.; Lu, J.; Kovochich, M.; Xia, T.; Ruehm, S. G.; Nel, A. E.; Tamanoi, F.; Zink, J. I. Multifunctional Inorganic Nanoparticles for Imaging, Targeting, and Drug Delivery. *ACS Nano* **2008**, *2*, 889–896.

(23) Terris, B. D.; Thomson, T. Nanofabricated and Self-Assembled Magnetic Structures as Data Storage Media. *J. Phys. D: Appl. Phys.* **2005**, *38*, R199.

(24) Loo, A. L.; Pineda, M. G.; Saade, H.; Treviño, M. E.; López, R. G. Synthesis of Magnetic Nanoparticles in Bicontinuous Microemulsions. Effect of Surfactant Concentration. *J Mater Sci* **2008**, *43*, 3649–3654.

(25) Kwon, S. G.; Hyeon, T. Colloidal Chemical Synthesis and Formation Kinetics of Uniformly Sized Nanocrystals of Metals, Oxides, and Chalcogenides. *Acc. Chem. Res.* **2008**, *41*, 1696–1709.

(26) Wu, W.; Wu, Z.; Yu, T.; Jiang, C.; Kim, W.-S. Recent Progress on Magnetic Iron Oxide Nanoparticles: Synthesis, Surface Functional Strategies and Biomedical Applications. *Sci. Technol. Adv. Mater.* **2015**, *16*, 023501.

(27) Park, J.; An, K.; Hwang, Y.; Park, J.-G.; Noh, H.-J.; Kim, J.-Y.; Park, J.-H.; Hwang, N.-M.; Hyeon, T. Ultra-Large-Scale Syntheses of Monodisperse Nanocrystals. *Nat Mater* **2004**, *3*, 891–895.

(28) Lodhia, J.; Mandarano, G.; Ferris, N.; Eu, P.; Cowell, S. Development and Use of Iron Oxide Nanoparticles (Part 1): Synthesis of Iron Oxide Nanoparticles for MRI. *Biomed Imaging Interv J* **2010**, *6*, e12.

(29) Wei, H.; Bruns, O. T.; Chen, O.; Bawendi, M. G. Compact Zwitterion-Coated Iron Oxide Nanoparticles for in Vitro and in Vivo Imaging. *Integr. Biol.* **2012**, *5*, 108–114.

(30) Jain, T. K.; Reddy, M. K.; Morales, M. A.; Leslie-Pelecky, D. L.; Labhasetwar, V. Biodistribution, Clearance, and Biocompatibility of Iron Oxide Magnetic Nanoparticles in Rats. *Mol. Pharmaceutics* **2008**, *5*, 316–327.

(31) Miguel-Sancho, N.; Bomatí-Miguel, O.; Colom, G.; Salvador, J.-P.; Marco, M.-P.; Santamaría, J. Development of Stable, Water-Dispersible, and Biofunctionalizable Superparamagnetic Iron Oxide Nanoparticles. *Chem. Mater.* **2011**, *23*, 2795–2802.

(32) Huang, Z.; Shen, Y.; Sun, A.; Huang, G.; Zhu, H.; Huang, B.; Xu, J.; Song, Y.; Pei, N.; Ma, J.; *et al.* Magnetic Targeting Enhances Retrograde Cell Retention in a Rat Model of Myocardial Infarction. *Stem Cell Res Ther* **2013**, *4*, 149.

(33) David, A. E.; Cole, A. J.; Chertok, B.; Park, Y. S.; Yang, V. C. A Combined Theoretical and in Vitro Modeling Approach for Predicting the Magnetic Capture and Retention of Magnetic Nanoparticles in Vivo. *J Control Release* **2011**, *152*, 67–75.

(34) Tan, R.; Blom, D. A.; Ma, S.; Greytak, A. B. Probing Surface Saturation Conditions in Alternating Layer Growth of CdSe/CdS Core/Shell Quantum Dots. *Chem. Mater.* **2013**, *25*, 3724–3736.

(35) García-Rodríguez, R.; Liu, H. Mechanistic Insights into the Role of Alkylamine in the Synthesis of CdSe Nanocrystals. *J. Am. Chem. Soc.* **2014**, *136*, 1968–1975.

(36) Chen, Y.; Vela, J.; Htoon, H.; Casson, J. L.; Werder, D. J.; Bussian, D. A.; Klimov, V. I.; Hollingsworth, J. A. "Giant" Multishell CdSe Nanocrystal Quantum Dots with Suppressed Blinking. *J. Am. Chem. Soc.* **2008**, *130*, 5026–5027.

(37) Guo, Y.; Marchuk, K.; Sampat, S.; Abraham, R.; Fang, N.; Malko, A. V.; Vela, J. Unique Challenges Accompany Thick-Shell CdSe/nCdS (n > 10) Nanocrystal Synthesis. *J. Phys. Chem. C* **2012**, *116*, 2791–2800.

(38) Foos, E. E.; Wilkinson, J.; Mäkinen, A. J.; Watkins, N. J.; Kafafi, Z. H.; Long, J. P. Synthesis and Surface Composition Study of CdSe Nanoclusters Prepared Using Solvent Systems Containing Primary, Secondary, and Tertiary Amines. *Chem. Mater.* **2006**, *18*, 2886–2894.

(39) Shen, Y.; Tan, R.; Gee, M. Y.; Greytak, A. B. Quantum Yield Regeneration: Influence of Neutral Ligand Binding on Photophysical Properties in Colloidal Core/Shell Quantum Dots. *ACS Nano* **2015**, *9*, 3345–3359.

(40) Talapin, D. V.; Rogach, A. L.; Kornowski, A.; Haase, M.; Weller, H. Highly Luminescent Monodisperse CdSe and CdSe/ZnS Nanocrystals Synthesized in a Hexadecylamine−Trioctylphosphine Oxide−Trioctylphospine Mixture. *Nano Lett.* **2001**, *1*, 207–211.

(41) Bullen, C.; Mulvaney, P. The Effects of Chemisorption on the Luminescence of CdSe Quantum Dots. *Langmuir* **2006**, *22*, 3007–3013.

(42) Jasieniak, J.; Smith, L.; Embden, J. van; Mulvaney, P.; Califano, M. Re-Examination of the Size-Dependent Absorption Properties of CdSe Quantum Dots. *J. Phys. Chem. C* **2009**, *113*, 19468–19474.

(43) Thessing, J.; Qian, J.; Chen, H.; Pradhan, N.; Peng, X. Interparticle Influence on Size/Size Distribution Evolution of Nanocrystals. *J. Am. Chem. Soc.* **2007**, *129*, 2736–2737.

(44) Kim, J. I.; Kim, J.; Lee, J.; Jung, D.-R.; Kim, H.; Choi, H.; Lee, S.; Byun, S.; Kang, S.; Park, B. Photoluminescence Enhancement in CdS Quantum Dots by Thermal Annealing. *Nanoscale Res Lett* **2012**, *7*, 482.

(45) Tonti, D.; van Mourik, F.; Chergui, M. On the Excitation Wavelength Dependence of the Luminescence Yield of Colloidal CdSe Quantum Dots. *Nano Lett.* **2004**, *4*, 2483–2487.

(46) Rumbles, G.; Selmarten, D. C.; Ellingson, R. J.; Blackburn, J. L.; Yu, P.; Smith, B. B.; Mićić, O. I.; Nozik, A. J. Anomalies in the Linear Absorption, Transient Absorption, Photoluminescence and Photoluminescence Excitation Spectroscopies of Colloidal InP Quantum Dots. *Journal of Photochemistry and Photobiology A: Chemistry* **2001**, *142*, 187–195.

(47) Hoy, J.; Morrison, P. J.; Steinberg, L. K.; Buhro, W. E.; Loomis, R. A. Excitation Energy Dependence of the Photoluminescence Quantum Yields of Core and Core/Shell Quantum Dots. *J. Phys. Chem. Lett.* **2013**, *4*, 2053–2060.

(48) Kambhampati, P. Hot Exciton Relaxation Dynamics in Semiconductor Quantum Dots: Radiationless Transitions on the Nanoscale. *J. Phys. Chem. C* **2011**, *115*, 22089–22109.

(49) Kambhampati, P. On the Kinetics and Thermodynamics of Excitons at the Surface of Semiconductor Nanocrystals: Are There Surface Excitons? *Chemical Physics* **2015**, *446*, 92–107.

(50) Minotto, A.; Todescato, F.; Fortunati, I.; Signorini, R.; Jasieniak, J. J.; Bozio, R. Role of Core–Shell Interfaces on Exciton Recombination in CdSe–CdxZn1–xS Quantum Dots. *J. Phys. Chem. C* **2014**, *118*, 24117–24126.

(51) Lakowicz, J. R. *Principles of Fluorescence Spectroscopy*; 3rd ed.; Springer: New York, 2006.

(52) Greytak, A. B.; Allen, P. M.; Liu, W.; Zhao, J.; Young, E. R.; Popović, Z.; Walker, B. J.; Nocera, D. G.; Bawendi, M. G. Alternating Layer Addition Approach to CdSe/CdS Core/shell Quantum Dots with near-Unity Quantum Yield and High on-Time Fractions. *Chem. Sci.* **2012**, *3*, 2028–2034.

(53) Kuno, M. Band Edge Spectroscopy of CdSe Quantum Dots. PhD Thesis, MIT, 1998.

(54) Wang, L.; Cole, M.; Li, J.; Zheng, Y.; Chen, Y. P.; Miller, K. P.; Decho, A. W.; Benicewicz, B. C. Polymer Grafted Recyclable Magnetic Nanoparticles. *Polym. Chem.* **2014**, *6*, 248–255.

APPENDIX A –COPYRIGHT PERMISSION

Appendix Copyright for Chapter 2

Copyright Clearance Center

RightsLink®

Home | Create Account | Help

ACS Publications
Most Trusted. Most Cited. Most Read.

Title: Reducing Competition by Coordinating Solvent Promotes Morphological Control in Alternating Layer Growth of CdSe/CdS Core/Shell Quantum Dots

Author: Rui Tan, Yi Shen, Stephen K. Roberts, et al

Publication: Chemistry of Materials

Publisher: American Chemical Society

Date: Nov 1, 2015

Copyright © 2015, American Chemical Society

LOGIN

If you're a copyright.com user, you can login to RightsLink using your copyright.com credentials. Already a RightsLink user or want to learn more?

PERMISSION/LICENSE IS GRANTED FOR YOUR ORDER AT NO CHARGE

This type of permission/license, instead of the standard Terms & Conditions, is sent to you because no fee is being charged for your order. Please note the following:

- Permission is granted for your request in both print and electronic formats, and translations.
- If figures and/or tables were requested, they may be adapted or used in part.
- Please print this page for your records and send a copy of it to your publisher/graduate school.
- Appropriate credit for the requested material should be given as follows: "Reprinted (adapted) with permission from (COMPLETE REFERENCE CITATION). Copyright (YEAR) American Chemical Society." Insert appropriate information in place of the capitalized words.
- One-time permission is granted only for the use specified in your request. No additional uses are granted (such as derivative works or other editions). For any other uses, please submit a new request.

BACK | CLOSE WINDOW